

Quantum gas mixtures and dual-species atom interferometry in space

<https://doi.org/10.1038/s41586-023-06645-w>

Received: 5 June 2023

Accepted: 14 September 2023

Published online: 15 November 2023

 Check for updates

Ethan R. Elliott¹✉, David C. Aveline¹, Nicholas P. Bigelow², Patrick Boegel³, Sofia Botsi¹, Eric Charron⁴, José P. D’Incao⁵, Peter Engels⁶, Timothé Estrampes^{4,7}, Naceur Gaaloul⁷, James R. Kellogg¹, James M. Kohel¹, Norman E. Lay¹, Nathan Lundblad⁸, Matthias Meister⁹, Maren E. Mossman^{6,10}, Gabriel Müller⁷, Holger Müller¹¹, Kamal Oudrhiri¹, Leah E. Phillips¹, Annie Pichery^{4,7}, Ernst M. Rasel⁷, Charles A. Sackett¹², Matteo Sbroscia¹, Wolfgang P. Schleich^{1,3,13,14,15}, Robert J. Thompson¹ & Jason R. Williams¹✉

The capability to reach ultracold atomic temperatures in compact instruments has recently been extended into space^{1,2}. Ultracold temperatures amplify quantum effects, whereas free fall allows further cooling and longer interactions time with gravity—the final force without a quantum description. On Earth, these devices have produced macroscopic quantum phenomena such as Bose–Einstein condensates (BECs), superfluidity, and strongly interacting quantum gases³. Terrestrial quantum sensors interfering the superposition of two ultracold atomic isotopes have tested the universality of free fall (UFF), a core tenet of Einstein’s classical gravitational theory, at the 10^{-12} level⁴. In space, cooling the elements needed to explore the rich physics of strong interactions or perform quantum tests of the UFF has remained elusive. Here, using upgraded hardware of the multiuser Cold Atom Lab (CAL) instrument aboard the International Space Station (ISS), we report, to our knowledge, the first simultaneous production of a dual-species BEC in space (formed from ⁸⁷Rb and ⁴¹K), observation of interspecies interactions, as well as the production of ³⁹K ultracold gases. Operating a single laser at a ‘magic wavelength’ at which Rabi rates of simultaneously applied Bragg pulses are equal, we have further achieved the first spaceborne demonstration of simultaneous atom interferometry with two atomic species (⁸⁷Rb and ⁴¹K). These results are an important step towards quantum tests of UFF in space and will allow scientists to investigate aspects of few-body physics, quantum chemistry and fundamental physics in new regimes without the perturbing asymmetry of gravity.

A growing infrastructure of space-based ultracold atomic physics has the potential for transformative discoveries in gravity science, cosmology, the nature of dark energy and dark matter, and quantum simulations of interacting many-body systems^{5–7}. Towards these objectives, a sub-orbital rocket payload has created BECs and performed atom interferometry in space^{1,8}, whereas the multiuser CAL, under remote operation from NASA’s Jet Propulsion Laboratory (JPL), has performed daily experiments based on ⁸⁷Rb BECs for the past 5 years aboard the ISS. CAL hardware support, provided by the NASA Astronaut Corps, has recently included two substantial upgrades to achieve matter-wave interferometry and sympathetic cooling of bosonic potassium. On Earth, future cold-atom devices bound for space are under active

development and testing, including the Bose-Einstein Condensate and Cold Atom Laboratory (BECCAL)⁹, the Cold Atom Physics Research Rack (CAPR)¹⁰ and the next MAIUS missions¹¹. Driving this growth is a remarkable interplay between ultracold temperatures and quantum phenomena that is enhanced by the microgravity conditions of space. For each benefit of microgravity to quantum science^{5,6}, there are new capabilities provided by the binary atomic mixtures described here.

Ultracold atomic systems are broadly used throughout the physical sciences^{12–14} for two key reasons: increased control over atomic behaviour and the amplification of quantum effects. The quantum wavelength of a massive particle is inversely related to its momentum, so by cooling an atom to temperatures within a millionth of a

¹Jet Propulsion Laboratory, California Institute of Technology, Pasadena, CA, USA. ²Department of Physics and Astronomy, University of Rochester, Rochester, NY, USA. ³Institut für Quantenphysik und Center for Integrated Quantum Science and Technology (IQST), Ulm University, Ulm, Germany. ⁴Institut des Sciences Moléculaires d’Orsay, Université Paris-Saclay, CNRS, Orsay, France. ⁵JILA, NIST, and the Department of Physics, University of Colorado, Boulder, CO, USA. ⁶Department of Physics and Astronomy, Washington State University, Pullman, WA, USA. ⁷Institute of Quantum Optics, QUEST-Leibniz Research School, Leibniz University Hannover, Hanover, Germany. ⁸Department of Physics and Astronomy, Bates College, Lewiston, ME, USA. ⁹German Aerospace Center (DLR), Institute of Quantum Technologies, Ulm, Germany. ¹⁰Department of Physics and Biophysics, University of San Diego, San Diego, CA, USA. ¹¹Department of Physics, University of California, Berkeley, CA, USA. ¹²Physics Department, University of Virginia, Charlottesville, VA, USA. ¹³Hagler Institute for Advanced Study, Texas A&M University, College Station, TX, USA. ¹⁴Texas A&M AgriLife Research, Texas A&M University, College Station, TX, USA. ¹⁵Institute for Quantum Science and Engineering (IQSE), Department of Physics and Astronomy, Texas A&M University, College Station, TX, USA. ✉e-mail: Ethan.R.Elliott@jpl.nasa.gov; Jason.R.Williams.Dr@jpl.nasa.gov

degree of absolute zero, the reduction in momentum causes the quantum wave to extend to micrometre length scales. By maturing the unique hardware required by these experiments to operate in space, microgravity-enhanced cooling techniques^{15,16} can create new regimes of ultralow temperatures, densities and free-space expansion rates^{17–19}. Given the appropriate atomic species and mixtures, these conditions are ideal for studying the emergence of complexity from controllable atomic systems, including quantum bubbles²⁰ and the formation of large and delicate quantum objects, such as Feshbach molecules²¹ or Efimov trimers^{22,23}. Further, a free-falling experimental apparatus extends the time that an unconfined quantum object has to interact with gravity before colliding with a surface of the device. These benefits compound for ultracold atom interferometers, which use light pulses to manipulate matter waves into an interfering quantum superposition at which the resulting phase difference can be affected by inertial forces such as gravity. The sensitivity of atom interferometry can scale with the square of time between light pulses⁵, a duration increased by slow expansion rates and extended free fall. A binary-BEC system in space allows an interferometer to simultaneously investigate the interaction of two quantum test masses with gravity, a critical step towards a quantum test of general relativity in space.

Einstein's classical theory of general relativity, our best description of gravity, is based on the UFF. The UFF requires that the trajectory of an object in space-time is independent of its composition. Although the legacy of experimentally testing this idea reaches back to the Renaissance, modern interest is sustained by theoretical attempts to reconcile quantum mechanics and gravity that lead to small UFF violations. Classically, this can be tested by measuring the differential acceleration between two test masses of different structure (that is, a boulder and a pebble), whereas the atom-interferometry analogue can use isotopically pure quantum test masses of different atomic species. On Earth, the most advanced atom-interferometry test of the UFF compared free-falling isotopes of ⁸⁷Rb and ⁸⁵Rb using a 10-m vacuum chamber and found no violation at the level of 10^{-12} (ref. 4). Recently, a 10^{-15} level of accuracy was achieved by a classical experiment within a satellite, capitalizing on the advantages of operating in space for precision UFF tests²⁴. Owing to the fundamental differences in the description of classical and quantum motion, combining these two research paths by studying several quantum test masses in space is a long-standing goal that has led to a variety of proposed missions^{9,25–28} and a terrestrial validation in atmospheric flight²⁹.

CAL at present serves as a multiuser facility to support the work of five science teams^{30–34}. Previous spaceborne experiments with BECs, adiabatic decompression, atom interferometry and unique microgravity topologies have relied solely on the atomic species ⁸⁷Rb (refs. 1,2,17,35–37). However, richer physics becomes accessible with the introduction of more diverse atomic species. Rubidium–potassium mixtures feature several intraspecies and interspecies collisional Feshbach resonances^{38–40}, in which an external magnetic field can be applied to continuously tune the strength of the collisional interaction and molecules can be adiabatically formed or dissociated without the sudden energy change typical of a chemical reaction⁴¹.

The subsystems and layout of the CAL instrument have been described previously^{2,42}. Upgrades and repairs are commonplace in an atomic-physics experiment, but the unique presence of CAL in space requires the intervention of the ISS crew for any hardware reconfiguration or repair. For this work, astronauts under guidance from a ground-support team at JPL have performed two key upgrades (Fig. 1). First, a new science module: CAL's full-vacuum chamber, atom source, coils and optics surrounded by magnetic shields. Fed by current sources and optical fibres, the new module features an extra fibre interface and internal optics to deliver light from an existing 785-nm laser for the purpose of Bragg interferometry. Second, a new microwave source for sympathetic cooling of the bosonic potassium isotopes ³⁹K and ⁴¹K. The new source features two independent synthesizers

for simultaneously addressing two internal states of ⁸⁷Rb and 38 dBm of output power. We first discuss the use of the microwave source to produce ultracold potassium.

CAL has the laser facilities to generate magneto-optical traps for both Rb and K. We use the favourable laser-cooling properties of ⁸⁷Rb and assign priority to the number of rubidium atoms loaded into our magnetic chip trap, with orders of magnitude fewer potassium atoms simultaneously confined as described in ref. 42. We then perform evaporative cooling on the rubidium atoms, in which the most energetic atoms are removed from the trap and the remainder rethermalize at a lower temperature. Our previous implementation of evaporative cooling worked by driving radiofrequency Zeeman transitions from trapped to untrapped spin states^{2,35,36}, which equally affects rubidium and potassium. However, a feature of microwave hyperfine transitions in alkali atoms is the fact that different elements, and even different isotopes, have transitions that are well separated from each other in their transition frequency. Therefore, using the newly installed microwave source, we can selectively drive transitions to remove only ⁸⁷Rb atoms, whereas potassium cools sympathetically through collisions with the actively cooled rubidium^{43–46} (Methods). These collisions, and the efficacy of sympathetic cooling, are parameterized by an interspecies scattering length. Although the scattering length between ⁸⁷Rb and ⁴¹K is favourably large ($163a_0$, in which a_0 is the Bohr radius), the scattering length between ⁸⁷Rb and ³⁹K is relatively small ($28a_0$)⁴⁰. Therefore, long evaporation times of tens of seconds have been required in previous Earth-based implementations to sympathetically cool ³⁹K with ⁸⁷Rb (refs. 45,47). Our system mitigates this problem with an atom-chip trap that is capable of generating strong confinement and thus a high collision rate. During the evaporative-cooling process, the trap frequencies are $(\omega_x, \omega_y, \omega_z)/2\pi = (26, 950, 950)$ Hz for ⁸⁷Rb and $(39, 1,420, 1,420)$ Hz for ³⁹K, with a trap bottom at a field of 10.03 G. Although this field is far from any known interspecies Feshbach resonance, this tight confinement allows us to perform microwave evaporation in 1.68 s. As a result, our setup allows us to sympathetically cool ³⁹K as well as ⁴¹K atoms with ⁸⁷Rb using just the magnetic trap, without the need to reload into an optical trap and exploit Feshbach resonances. This simplifies the procedure and hardware—a notable advantage for spaceborne applications.

Although the microwave cooling of ⁸⁷Rb is a powerful technique, the required microwave power and ⁸⁷Rb atoms populating the $|2, 1\rangle$ state creates further challenges even without the presence of a second species. In response, the full capabilities of the upgraded multitone microwave source were crucial to producing ⁸⁷Rb condensates in the $|2, 2\rangle$ state, with the atom number exceeding 1.5×10^4 (Methods). We first demonstrated sympathetic cooling of ³⁹K, with natural abundance of approximately 93.3% compared with an abundance of 6.7% for ⁴¹K. A larger abundance generally favours the initial loading of atoms into a magneto-optical trap, thus providing a more favourable starting point for subsequent cooling steps. Loading ⁸⁷Rb and ³⁹K into the chip trap and evaporating with the same microwave protocol used to produce a pure ⁸⁷Rb BEC led to a faint ³⁹K signal of only a few hundred atoms. However, by reoptimizing the microwave evaporation procedure (Methods), we were able to produce 3×10^4 ³⁹K atoms at 350 nK, as shown in Fig. 2c. We note that ³⁹K in the $|2, 2\rangle$ state has a negative background scattering length, which prevents a stable BEC near zero field. At present, CAL is designed to only study non-condensed ultracold samples of this species (Methods).

We then investigated cooling ⁴¹K to degeneracy. Using the same microwave evaporation protocol for ³⁹K, we produced the ⁴¹K BEC shown in Fig. 2b, with no ⁸⁷Rb remaining. In optimizing for a binary BEC of ⁸⁷Rb and ⁴¹K, we encountered the expected strong anticorrelation in atom number for each species⁴⁸. With further adjustments to the evaporation sequence (Methods), we were able to restore sufficient ⁸⁷Rb population to produce the binary BEC shown in Fig. 2a. The final evaporation stage yields typically 1.3×10^4 degenerate rubidium atoms

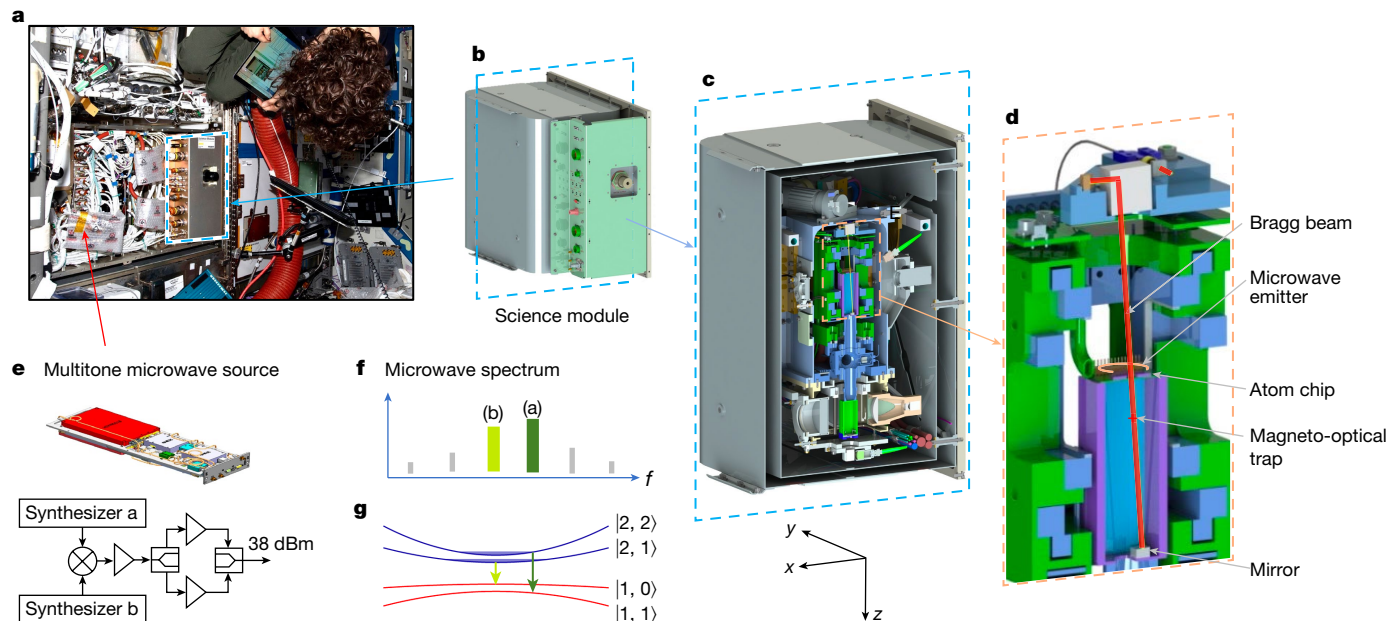


Fig. 1 | CAL on-orbit hardware upgrades. **a**, The CAL payload, housed in EXPRESS Rack 7 in the U.S. Lab Destiny Module of the ISS, undergoing preparation for removal of the original science module, designated SM2, which launched with CAL in 2018 (image source: NASA). SM2 was used for the results reported in refs. 2, 17, 35, 36 and replaced with science module SM3 by the ISS crew in January 2020 (astronaut Christina Koch pictured). The new capabilities of SM3 and an upgraded multitone microwave source were both necessary for the current results. **b**, SM3, containing atom-interferometry optics not present in SM2, and a new atom-chip layout (Extended Data Fig. 3). **c**, A cross-section of SM3 showing the vacuum chamber in which atom cooling and interferometry occurs (purple). **d**, Enlarged view of the atom-interferometry platform above the vacuum chamber. Exiting an optical fibre, the red line indicates the path of the 1-mm-diameter Bragg beam, propagating approximately along the direction

of Earth's gravity vector (z direction) within the vacuum chamber. **e**, The multitone microwave source installed in July 2021, with simplified block diagram. Synthesizer b gives a dynamically tunable output at 6.8–7.2 GHz, whereas synthesizer a provides the same at 0–60 MHz. Their mixed output is split and amplified before recombination to maximize available power in the upper harmonics. When maximum single-tone power is required at the start of evaporation (Methods), synthesizer b is operated alone in a sweep above 6.86 GHz and 38 dBm to transfer ^{87}Rb atoms in the $|2, 2\rangle$ state to the state $|1, 1\rangle$. In a later stage, synthesizers b and a are operated simultaneously near 6.84 GHz and 14 MHz, respectively, to give the spectrum shown in **f**. Further mixing harmonics are shown in grey. In this configuration, tone (b) removes ^{87}Rb atoms in the state $|2, 1\rangle$, whereas sideband (a) sweeps to evaporate atoms from the $|2, 2\rangle$ state to the $|1, 1\rangle$ state, as shown in **g**.

and 1.5×10^3 degenerate potassium atoms. With this performance, we investigate the behaviour of the binary quantum mixture and perform dual-species atom interferometry.

The mean-field interaction between ^{87}Rb and ^{41}K atoms is repulsive at low fields, making condensates of the two species generally immiscible⁴⁴. On Earth, the greater ^{87}Rb mass results in a ^{87}Rb condensate that is typically located below the ^{41}K condensate. Starting from a system of coupled Gross–Pitaevskii equations to investigate the ground state of the two magnetically confined BECs in microgravity, we obtain a near degeneracy between possible symmetric and asymmetric configurations of the condensates. Following the techniques of ref. 49 to propagate this model through stages of decompression and free expansion, we find that the different initial states are indistinguishable by the time we image. Instead, we find that the greatest influence of interspecies interactions on the observed BEC positions occur during the dynamics of decompression and release from the atom-chip trap. We plot the model results at the time of imaging for comparison with the data in Fig. 3. The measured BEC components are well matched to the model, with Fig. 3c,d further showing that the presence of both BECs correlates to a shift in the condensed ^{41}K atoms relative to the centre of the non-condensed ^{41}K thermal distribution. This is in contrast to the case of a single ^{41}K BEC (Fig. 3e,f). A similar shift has been observed in terrestrial studies of condensed ^{41}K and ^{87}Rb mixtures⁴⁹. Because the non-condensed atoms have no marked mean-field interactions compared with the condensates, this displacement between the thermal and condensed components is a signature of interaction effects, providing the first evidence for interspecies interactions of degenerate matter

in space. These effects will be the subject of further studies, in which we aim to experimentally distinguish the ground-state configurations of the trapped atoms.

To explore the feasibility of near-term quantum tests of the equivalence principle in space, we performed simultaneous atom interferometry on ^{41}K and ^{87}Rb BECs. CAL uses Bragg scattering⁵⁰ to provide the required atomic-beam splitting and reflection operations, in which the atomic wavefunctions interact with an optical lattice produced by off-resonant counter-propagating laser beams. A two-photon transition places the wavefunction in a superposition of different momentum states, maintaining the same internal state. By remaining in the same internal state, differential effects such as ac Stark shifts or Zeeman shifts are highly suppressed. As shown in Fig. 1, the lattice laser, or Bragg beam, enters the vacuum cell through a window at the centre of the atom chip and is retro-reflected by a mirror inside the cell. The path is nominally aligned with the direction of Earth's gravity vector. The maximum laser power is 66 mW and the wavelength is 785 nm.

Because changing the momentum of an atom changes its kinetic energy, driving a Bragg transition efficiently requires a time-dependent potential. We tailor the release of atoms from the magnetic trap in the $|2, 2\rangle$ state to give the ^{87}Rb and ^{41}K cloud velocities of 1.2 cm s^{-1} and 1.9 cm s^{-1} , respectively, along the Bragg laser beam. In this way, the degeneracy that would otherwise allow transitions among momentum states to be driven simultaneously in two directions is broken. This preparation scheme results in Bragg resonance frequencies of 48 kHz for ^{87}Rb and 88 kHz for ^{41}K (see Extended Data Fig. 2). The Bragg laser is

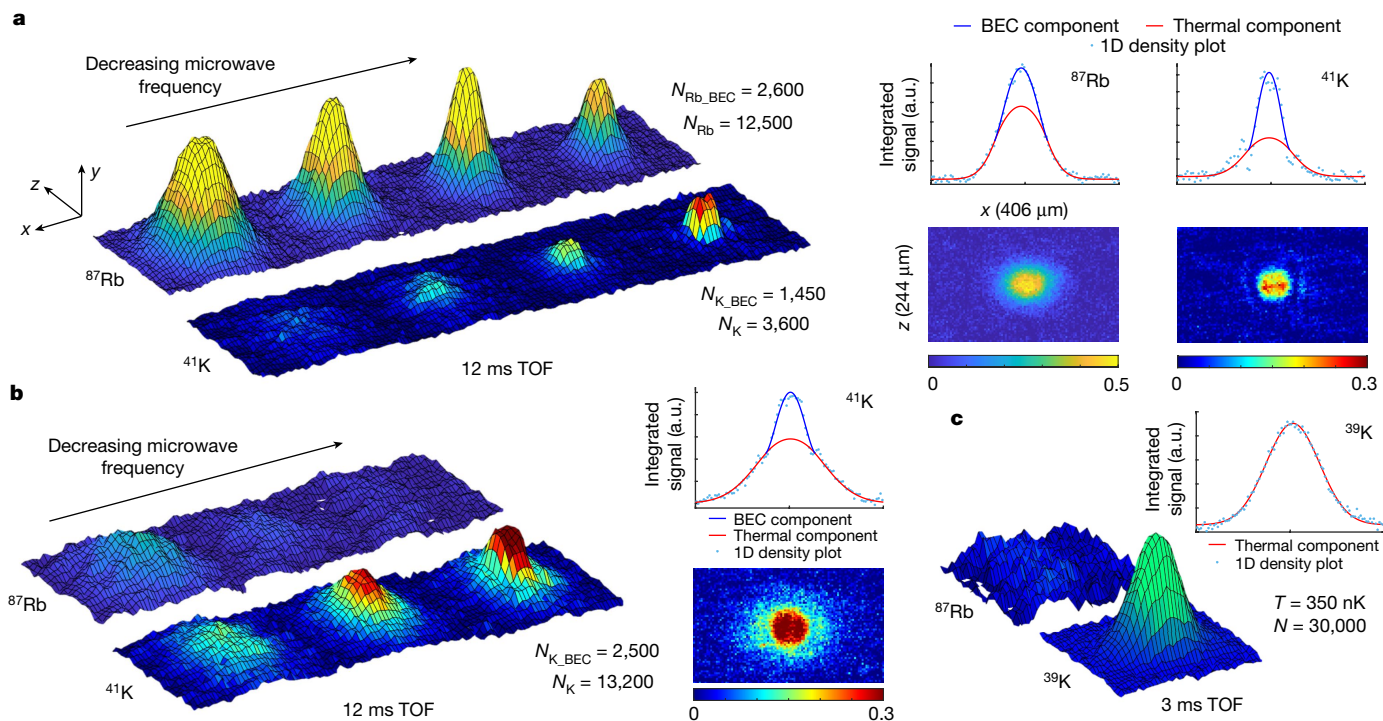


Fig. 2 | Production of degenerate quantum mixtures in space. False-colour absorption images of ^{87}Rb , ^{41}K and ^{39}K atomic clouds following microwave evaporation, decompression and release from the magnetic chip trap of CAL (Methods). All images are $244 \times 406 \mu\text{m}$ (60×100 pixels) in the z and x directions, respectively. The potassium cloud is imaged following the indicated time of flight in free expansion (TOF) and a separate laser frequency images ^{87}Rb 2.1 ms later. The vertical axis of all 3D surface plots is optical density and height is referenced to a common scale with a maximum of 3.5. Each atomic species then has a separate relation between height and colour, in which a different false-colour map is assigned to each species, with the colour limits corresponding to the optical density ranges indicated. **a**, Preparation of a dual-species degenerate gas. From left to right, the final frequency of an evaporative cooling ramp using a multitone microwave source is lowered, with the microwave evaporation

supplemented by an extra radiofrequency source. In this example, ^{87}Rb condenses first at a critical temperature of 70 nK (second from left). The final evaporation step lowers the ^{87}Rb temperature to 46 nK, remaining below a lower critical temperature, whereas the atom number drops to 1.25×10^4 , simultaneously producing a ^{41}K BEC with 1.45×10^3 atoms at 37 nK. Temperatures are calculated from the measured BEC fraction, atom number and trap frequencies. 1D density plots (light-blue points) show the bimodal fit for the BEC (blue) and thermal (red) components in the final evaporation stage. **b**, Potassium performance given priority by evaporating with only microwaves and a ^{87}Rb BEC never forms. ^{41}K atom number is maintained at about 1.32×10^4 in each image as the critical temperature of 95 nK is passed (middle), with a final temperature of 70 nK (right). **c**, ^{39}K sympathetically cooled to ultracold temperatures, with no ^{87}Rb remaining. a.u., arbitrary units.

controlled by an acousto-optic modulator (AOM), which can provide three simultaneous frequency components. For single-species operation, two components are used, separated by the corresponding Bragg frequency. Using all three components, both species can be addressed at any velocity simultaneously.

To calibrate the Bragg interaction, we first measured Rabi rates for each Bragg transition in the two-tone configuration, implemented single-species Mach–Zehnder interferometers (Methods) and then recalibrated in the tritone configuration for dual-species interferometry (see Extended Data Fig. 1). The power ratio of the frequency components was adjusted slightly to give equal Rabi rates and a shared $\pi/2$ time of 0.27 ms for both species. The three-pulse Mach–Zehnder interferometer was then applied with $T = 0.5$ ms. The results, shown in Fig. 4, exhibit clear interference in both species with measured visibilities of 0.16 ± 0.03 for ^{41}K and 0.15 ± 0.03 for ^{87}Rb , in excellent agreement with predictions accounting for the efficiencies of each Bragg pulse (Methods). A differential phase measurement result of $0.4^{+0.5}_{-1.2}$ fulfils expectations as a starting point for future quantum tests of the UFF in space.

Building on this proof-of-principle demonstration, CAL teams are working to realize the full performance of the instrument’s dual-species atom interferometry. In outlining relevant next steps, we note that a common Bragg beam for all atomic species gives excellent potential for suppressing common-mode noise⁵¹. In a first on Earth or in space, the

Bragg beam was chosen to be near a ‘magic wavelength’ at which the Rabi rates for rubidium and potassium are equal. A shared Bragg beam minimizes perturbations from laser frequency noise, laser intensity fluctuations and vibrations of the ISS (ref. 27). Experimental constraints that at present limit the sensor performance in terms of visibility and achievable atom-interferometry interrogation time derive mainly from imperfections in the positional overlap between the Bragg laser beam and the atomic samples during atom interferometry. The moderate Bragg beam size, with $1/e^2$ waist approximately 0.5 mm, requires: (1) increasing precision in the release of rubidium and potassium gases with respect to the beam centre; (2) reduction of the expansion energy of the gases to maintain overlap of the Bragg beam profile as time of flight increases; and (3) increasing environmental control over residual forces acting on the atoms. Doppler widths of the gases are at present on par with the maximum two-photon Rabi frequencies for Bragg transitions (both species), but atom temperature is not expected to be the limiting factor. Effective temperatures as low as 52 pK have been demonstrated with ^{87}Rb in CAL (ref. 17), allowing visibility on the timescale of seconds, and similar efforts are continuing for dual-species mixtures. Rather, it is the rotation of the ISS, at an orbital period of 91 min, that will limit atom-interferometry fringe visibility even at $T = 500$ ms (ref. 32). For this reason, future Earth-orbiting missions plan to maintain interferometer visibility with internal rotation compensation⁹. With near-term work dedicated to cooling dual-species gases to sub-nK temperatures,

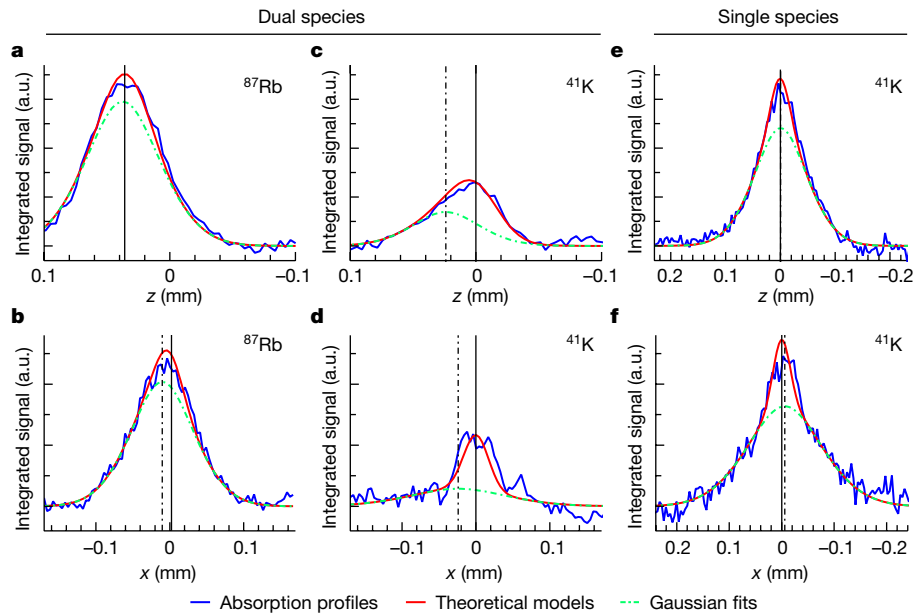


Fig. 3 | Interactions of degenerate ^{87}Rb and ^{41}K mixtures. Blue traces are ^{87}Rb and ^{41}K absorption profiles from the final evaporation stages of Fig. 2a,b, integrated along the x and z directions, respectively. Red traces are theoretical models obtained by solving for the ground-state configuration of the trap and then propagating the initial states through the processes of trap decompression, release and free expansion. The distributions are convolved with a $15\text{-}\mu\text{m}$ Gaussian to account for the resolution of the camera. Position 0 is defined as the centre of the condensate component for ^{41}K , in which the positive z direction points away from the chip, consistent across figures. The solid vertical lines show the centre position of the condensate component for each species. Dashed green traces are Gaussian fits to the data, showing the

non-condensed atoms in the gas. The dashed vertical lines show the centre of the non-condensed component. The position fit has a 1σ confidence bound that fluctuates from 0.2 to $1.4\text{ }\mu\text{m}$. For the dual-species cases, the distance between the position of the Thomas–Fermi fit of the condensed cloud and the Gaussian fit of the thermal cloud are for $\text{Rb } \Delta z_{\text{Rb}} = 1.6\text{ }\mu\text{m}$ (a) and $\Delta x_{\text{Rb}} = 12.4\text{ }\mu\text{m}$ (b) and for the K cloud $\Delta z_{\text{K}} = 24.0\text{ }\mu\text{m}$ (c) and $\Delta x_{\text{K}} = 24.0\text{ }\mu\text{m}$ (d). These displacements are consistent with model calculations that take into account mean-field interactions between the two condensates. When no ^{87}Rb is present, the overlap of the ^{41}K condensate and the ^{41}K thermal component is restored, with $\Delta z_{\text{K}} = -0.4\text{ }\mu\text{m}$ (e) and $\Delta x_{\text{K}} = -5.8\text{ }\mu\text{m}$ (f). a.u., arbitrary units.

preparation into magnetically insensitive (for example, $|2, 0\rangle$) states and advanced control over the cloud centre of mass motion^{17,35}, it is expected that fringe visibility at interrogation times in the hundreds of milliseconds range will be achievable. Following campaigns to increase interrogation time, relating differential interferometer phase to the

UFF requires dedicated measurements characterizing the full range of systematic errors. Finally, we note the limited signal-to-noise ratio in imaging clouds with thousands of atoms in extended free fall. For quantum UFF tests to take full advantage of space and set new records of sensitivity, estimates require atom numbers greater than 10^6 per

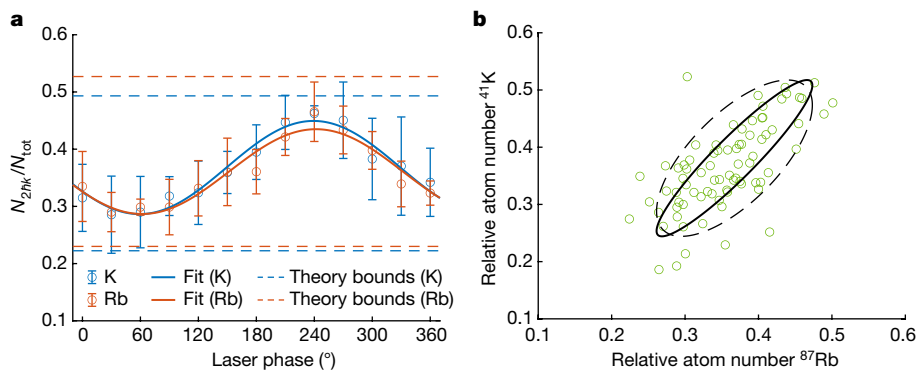


Fig. 4 | Dual-species atom interferometry in space. a, Normalized population for ultracold samples of ^{41}K (blue) and ^{87}Rb (red) in the excited momentum state $2hk$ following the application of three Bragg pulses in a Mach–Zehnder configuration. The time between pulses is $T = 0.5\text{ ms}$ and the pulse durations are $270\text{ }\mu\text{s}$, $580\text{ }\mu\text{s}$ and $270\text{ }\mu\text{s}$, respectively. Each pulse interacts with both atomic species simultaneously and contains three frequency components configured to drive Bragg transitions in both species with equal Rabi rates. For the third pulse, the same variable phase shift ($^\circ$) is applied to components addressing each species, in steps of 30° . Interference causes the population of the output states to vary sinusoidally, as observed. The offset and amplitude of the oscillation agrees very well with the expected minimal and maximal

populations in the excited momentum state (dashed lines) obtained by modelling the efficiencies of all three pulses (Methods). Each data point and error bar represents the average and standard deviation of between 5 and 15 independent experimental runs, respectively, for a chosen phase shift. b, Comparison of the relative population in the excited momentum state of ^{41}K and ^{87}Rb showing a correlation between both species. Fitting an ellipse (solid black ellipse) to the data yields a vanishing differential phase of $0.4^{+0.5}_{-1.2}$, indicating that both interferometers measured the same phase. The dashed black ellipse illustrates the phase uncertainty of the fit (Methods). For comparison, the individual phases are found to be 1.03 ± 0.08 for ^{41}K and 1.08 ± 0.10 for ^{87}Rb .

species²⁸, exceeding the best terrestrial performance at $>10^5$ per species⁵². Increasing the baseline atom number is a continuing and necessary technology development process, within CAL and future missions^{9,11,28}.

In summary, we have commissioned the upgraded capabilities of the CAL instrument to form quantum-gas mixtures in low-Earth orbit, including the condensation of ^{41}K and ^{87}Rb to form the first dual-species BECs in space, the observation of interspecies interactions and the preparation of ultracold ^{39}K . We have also achieved dual-species atom interferometry in space, using simultaneous Bragg interferometry of ^{87}Rb and ^{41}K with a single laser interrogating both species at the magic wavelength. This work is pursued by CAL investigators as a direct pathfinder for future precision measurements with atom interferometers, including quantum tests of the UFF in space, spectroscopic mass measurements through photon recoil and the direct detection of candidate sources to explain dark-sector physics^{30,32,34}. It further provides a platform for investigating new few-body and many-body physics phenomena in the absence of gravitational perturbations. For instance, tuning interactions by means of homonuclear (^{39}K) or heteronuclear (^{41}K + ^{87}Rb) Feshbach resonances in combination with extremely low-energy regimes can be used to form weakly bound two-atom or three-atom molecules with large spatial extent. Such work is already underway on CAL for testing the universality of Efimov physics³¹ and deploying heteronuclear molecules as a source of atomic mixtures with overlapping spatial distributions^{32,53}. CAL scientists also plan to study the emergence of structure and complexity in the absence of gravity by means of dual-species gases confined in shell-shaped potentials created by either radiofrequency dressing³³ or the stabilized interactions of immiscible heteronuclear gases^{17,30}. In the near term, it is anticipated that space-enabled studies of quantum systems will include quantum droplets⁵⁴, matter-wave interferometry with halo molecules of large spatial extent to explore the fundamental limits of superposition^{55–57}, the collisional dynamics of interacting dual-species gases⁴⁹ and molecular dissociation as a source of motionally entangled atoms⁵⁵. The confluence of quantum mixtures, large molecules, matter-wave interferometry and microgravity will be a powerful method for precision metrology, quantum simulation and cosmology, and testing the foundations of modern-day fundamental physics.

Online content

Any methods, additional references, Nature Portfolio reporting summaries, source data, extended data, supplementary information, acknowledgements, peer review information; details of author contributions and competing interests; and statements of data and code availability are available at <https://doi.org/10.1038/s41586-023-06645-w>.

- Becker, D. et al. Space-borne Bose–Einstein condensation for precision interferometry. *Nature* **562**, 391–395 (2018).
- Aveline, D. C. et al. Observation of Bose–Einstein condensates in an Earth-orbiting research lab. *Nature* **582**, 193–197 (2020).
- Levin, K., Fetter, A. L. & Stamper-Kurn, D. M. *Ultracold Bosonic and Fermionic Gases* (Elsevier, 2012).
- Asenbaum, P., Overstreet, C., Kim, M., Curti, J. & Kasevich, M. A. Atom-interferometric test of the equivalence principle at the 10^{-12} level. *Phys. Rev. Lett.* **125**, 191101 (2020).
- Safronova, M. et al. Search for new physics with atoms and molecules. *Rev. Mod. Phys.* **90**, 025008 (2018).
- Bassi, A. et al. A way forward for fundamental physics in space. *npj Microgravity* **8**, 49 (2022).
- Alonso, I. et al. Cold atoms in space: community workshop summary and proposed road-map. *EPJ Quantum Technol.* **9**, 30 (2022).
- Lachmann, M. D. et al. Ultracold atom interferometry in space. *Nat. Commun.* **12**, 1317 (2021).
- Frye, K. et al. The Bose–Einstein condensate and cold atom laboratory. *EPJ Quantum Technol.* **8**, 1 (2021).
- Li, L. et al. The design, realization, and validation of the scheme for quantum degenerate research in microgravity. *IEEE Photonics J.* **15**, 1–8 (2023).
- Elsen, M. et al. A dual-species atom interferometer payload for operation on sounding rockets. *Microgravity Sci. Technol.* **35**, 15 (2023).
- Bloch, I., Dalibard, J. & Nascimbène, S. Quantum simulations with ultracold quantum gases. *Nat. Phys.* **8**, 267–276 (2012).
- Braaten, E. & Hammer, H. W. Universality in few-body systems with large scattering length. *Phys. Rep.* **428**, 259–290 (2006).
- Salomon, C., Shlyapnikov, G. V. & Cugliandolo, L. F. *Many-Body Physics with Ultracold Gases: Lecture Notes of the Les Houches Summer School* (Oxford Univ. Press, 2012).
- Leanhardt, A. E. et al. Cooling Bose–Einstein condensates below 500 picokelvin. *Science* **301**, 1513–1515 (2003).
- Ammann, H. & Christensen, N. Delta kick cooling: a new method for cooling atoms. *Phys. Rev. Lett.* **78**, 2088–2091 (1997).
- Gaaloul, N. et al. A space-based quantum gas laboratory at picokelvin energy scales. *Nat. Commun.* **13**, 7889 (2022).
- Deppner, C. et al. Collective-mode enhanced matter-wave optics. *Phys. Rev. Lett.* **127**, 100401 (2021).
- Kovachy, T. et al. Matter wave lensing to picokelvin temperatures. *Phys. Rev. Lett.* **114**, 143004 (2015).
- Wolf, A. et al. Shell-shaped Bose–Einstein condensates based on dual-species mixtures. *Phys. Rev. A* **106**, 013309 (2022).
- Chin, C., Grimm, R., Julienne, P. & Tiesinga, E. Feshbach resonances in ultracold gases. *Rev. Mod. Phys.* **82**, 1225–1286 (2010).
- Chapurin, R. et al. Precision test of the limits to universality in few-body physics. *Phys. Rev. Lett.* **123**, 233402 (2019).
- Xie, X. et al. Observation of Efimov universality across a nonuniversal Feshbach resonance in ^{39}K . *Phys. Rev. Lett.* **125**, 243401 (2020).
- Touboul, P. et al. MICROSCOPE mission: final results of the test of the equivalence principle. *Phys. Rev. Lett.* **129**, 121102 (2022).
- Amelino-Camelia, G. et al. GAUGE: the GrAnd Unification and Gravity Explorer. *Exp. Astron.* **23**, 549–572 (2009).
- Schuldt, T. et al. Design of a dual species atom interferometer for space. *Exp. Astron.* **39**, 167–206 (2015).
- Williams, J. R., Chiow, S.-W., Yu, N. & Müller, H. Quantum test of the equivalence principle and space-time aboard the international space station. *New J. Phys.* **18**, 025018 (2016).
- Ahlers, H. et al. STE-QUEST: Space Time Explorer and QUantum Equivalence principle Space Test. Preprint at <https://arxiv.org/abs/2211.15412> (2022).
- Barrett, B. et al. Dual matter-wave inertial sensors in weightlessness. *Nat. Commun.* **7**, 13786 (2016).
- Bigelow, N. Consortium for Ultracold Atoms in Space. <https://taskbook.nasaprs.com/tbpdf.cfm?id=10085> (2015).
- Cornell, E. Zero-G Studies of Few-Body and Many-Body Physics. <https://taskbook.nasaprs.com/tbpdf.cfm?id=11096> (2017).
- Williams, J. Fundamental Interactions for Atom Interferometry with Ultracold Quantum Gases in a Microgravity Environment. <https://taskbook.nasaprs.com/tbpdf.cfm?id=11101> (2017).
- Lundblad, N. Microgravity Dynamics of Bubble-Geometry Bose–Einstein Condensates. <https://taskbook.nasaprs.com/tbpdf.cfm?id=11095> (2017).
- Sackett, C. Development of Atom Interferometry Experiments for the International Space Station's Cold Atom Laboratory. <https://taskbook.nasaprs.com/tbpdf.cfm?id=11097> (2017).
- Pollard, A. R., Moan, C. A., Sackett, C. A., Elliott, E. R. & Thompson, R. J. Quasi-adiabatic external state preparation of ultracold atoms in microgravity. *Microgravity Sci. Technol.* **32**, 1175–1184 (2020).
- Carollo, R. A. et al. Observation of ultracold atomic bubbles in orbital microgravity. *Nature* **606**, 281–286 (2022).
- Williams, J. R. et al. Interferometry of atomic matter-waves in a Cold Atom Lab onboard the International Space Station (in preparation).
- Inouye, S. et al. Observation of heteronuclear Feshbach resonances in a mixture of bosons and fermions. *Phys. Rev. Lett.* **93**, 183201 (2004).
- Klempt, C. et al. ^{40}K – ^{87}Rb Feshbach resonances: modeling the interatomic potential. *Phys. Rev. A* **76**, 020701 (2007).
- Ferlaino, F. et al. Feshbach spectroscopy of a K–Rb atomic mixture. *Phys. Rev. A* **73**, 040702 (2006).
- Timmermans, E. M. E., Tommasini, P., Hussein, M. S. & Kerman, A. K. Feshbach resonances in atomic Bose–Einstein condensates. *Phys. Rep.* **315**, 199–230 (1999).
- Elliott, E. R., Krutzik, M. C., Williams, J. R., Thompson, R. J. & Aveline, D. C. NASA's Cold Atom Lab (CAL): system development and ground test status. *npj Microgravity* **4**, 16 (2018).
- Modugno, G. et al. Bose–Einstein condensation of potassium atoms by sympathetic cooling. *Science* **294**, 1320–1322 (2001).
- Modugno, G., Modugno, M., Riboli, F., Roati, G. & Inguscio, M. Two atomic species superfluid. *Phys. Rev. Lett.* **89**, 190404 (2002).
- Campbell, R. et al. Efficient production of large ^{39}K Bose–Einstein condensates. *Phys. Rev. A* **82**, 063611 (2010).
- Wacker, L. et al. Tunable dual-species Bose–Einstein condensates of ^{39}K and ^{87}Rb . *Phys. Rev. A* **92**, 053602 (2015).
- Roati, G. et al. ^{39}K Bose–Einstein condensate with tunable interactions. *Phys. Rev. Lett.* **99**, 010403 (2007).
- Burchianti, A. et al. Dual-species Bose–Einstein condensate of ^{41}K and ^{87}Rb in a hybrid trap. *Phys. Rev. A* **98**, 063616 (2018).
- Pichery, A. et al. Efficient numerical description of the dynamics of interacting multispecies quantum gases. Preprint at <https://doi.org/10.48550/arXiv.2305.13433> (2023).
- Kozuma, M. et al. Coherent splitting of Bose–Einstein condensed atoms with optically induced Bragg diffraction. *Phys. Rev. Lett.* **82**, 871–875 (1999).
- Chiow, S.-W., Williams, J. & Yu, N. Noise reduction in differential phase extraction of dual atom interferometers using an active servo loop. *Phys. Rev. A* **93**, 013602 (2016).
- Cavicchioli, L., Fort, C., Modugno, M., Minardi, F. & Burchianti, A. Dipole dynamics of an interacting bosonic mixture. *Phys. Rev. Res.* **4**, 043068 (2022).

53. D'Incao, J. P., Krutzik, M., Elliott, E. & Williams, J. R. Enhanced association and dissociation of heteronuclear Feshbach molecules in a microgravity environment. *Phys. Rev. A* **95**, 012701 (2017).
54. Engles, P., Bisset, R. N., D'Incao, J., Forbes, M. M. & Mossman, M. E. Topical: Fundamental Physics and Opportunities with Ultracold Quantum Droplets in Space. https://smd-cms.nasa.gov/wp-content/uploads/2023/05/231_3b2a5a757441d7f3fc94f60661efc284_EngelsPeter.pdf (2021).
55. D'Incao, J. P. et al. Perspectives and opportunities: a molecular toolkit for fundamental physics and matter-wave interferometry in microgravity. *Quantum Sci. Technol.* **8**, 014004 (2022).
56. Chapman, M. S. et al. Optics and interferometry with Na₂ molecules. *Phys. Rev. Lett.* **74**, 4783–4786 (1995).
57. Penrose, R. On the gravitization of quantum mechanics 1: quantum state reduction. *Found. Phys.* **44**, 557–575 (2014).

Publisher's note Springer Nature remains neutral with regard to jurisdictional claims in published maps and institutional affiliations.

Springer Nature or its licensor (e.g. a society or other partner) holds exclusive rights to this article under a publishing agreement with the author(s) or other rightsholder(s); author self-archiving of the accepted manuscript version of this article is solely governed by the terms of such publishing agreement and applicable law.

© The Author(s), under exclusive licence to Springer Nature Limited 2023

Methods

Microwave evaporation

To optimally load our magnetic trap and achieve tight confinement for efficient evaporation, we trap and evaporate ^{87}Rb , ^{41}K and ^{39}K in the $|F=2, m_F=2\rangle$ state, in which coupling to the magnetic trap is strongest. The starting atom number and collision rate from this state is crucial for sympathetically cooling ^{39}K using just the magnetic trap. However, in this state, ^{39}K has a negative background scattering length, which prevents a stable BEC. Although adjusting the scattering length to form a ^{39}K BEC without an optical trap is a challenge that could potentially be overcome with a dedicated campaign, planned studies of extremely large and loosely bound Efimov states with ^{39}K in CAL require the ultralow densities and temperatures achievable through microgravity-enhanced adiabatic processes, not a degenerate gas. With the availability of ^{41}K , which has a favourable interspecies and intraspecies scattering length for forming a BEC in the presence of ^{87}Rb , there are no plans to perform interferometry with a ^{39}K BEC. For these reasons, a ^{39}K BEC was not part of the original CAL design. We further note that, with ^{87}Rb in the $|2, 2\rangle$ state, any ^{39}K that is co-trapped while occupying the lowest hyperfine state leads to severe losses. However, once the evaporation/sympathetic cooling stage of ^{87}Rb and ^{39}K in the $|2, 2\rangle$ state has concluded, the CAL instrument does have the capabilities to then transfer ^{87}Rb , ^{39}K or ^{41}K to their lowest hyperfine states (with ^{87}Rb being transferred first to avoid the aforementioned losses), as required for specific applications.

The microwave source features a tunable synthesizer operating in a range near 6.8 GHz, which can be mixed with the output of a second synthesizer operating from 4 to 50 MHz. Operating at a single tone, the maximum output power is 38 dBm. ^{87}Rb atoms in both the $|F, m_F=|2, 2\rangle$ and the $|2, 1\rangle$ Zeeman states can be magnetically trapped, whereas uncooled $|2, 1\rangle$ atoms are a source of heating. Further, they can collide inelastically with K, which ejects both atoms from the trap⁵⁸. A single microwave tone cannot simultaneously interact with both states, so it is necessary to separately drive both $|2, 2\rangle$ and $|2, 1\rangle$ states to an untrapped state using several frequencies. The multitone capability of the new microwave source accommodates this. However, spreading the microwave spectrum over several frequencies reduces the power available to drive any single transition. For pure ^{87}Rb evaporation, an initial cooling stage used a single tone to drive the $|2, 2\rangle \rightarrow |1, 1\rangle$ transition. In a later stage, the multitone output was used with the carrier driving the $|2, 1\rangle \rightarrow |1, 0\rangle$ transition, whereas a sideband cooled the $|2, 2\rangle$ state. Powers were 29 dBm in the carrier and 33 dBm in the sideband. To sympathetically cool K atoms, it was crucial to remove the $|2, 1\rangle$ Rb atoms quickly and efficiently. We achieved this through a combination of periodically jumping the single-tone output to the $|2, 1\rangle$ trap bottom during the first stage and switching to the multitone output sooner.

To produce dual-species condensates, it was necessary to preserve more of the Rb atoms during evaporation. We achieved this by adding an extra radiofrequency field set to be resonant with the Zeeman transition at a field about 5 G (equivalent to 300 μK) higher in the magnetic trap than where the microwave tones were resonant. This increased the final atom number by about 20% even for pure Rb evaporation. We attribute this benefit to the presence of hotter atoms in the trap that the microwave tone has missed, which the radiofrequency field prevents from thermalizing with the colder atoms at the trap bottom^{59,60}. A second possible explanation is an effective power increase in the microwave transition owing to a double-dressing of the ^{87}Rb atoms by the microwave and radiofrequency frequencies⁶¹, but we did not directly observe any effect of the radiofrequency field on the microwave Rabi frequency. Adding the radiofrequency field also reduced the final amount of ^{41}K , probably because it ejected some warmer K atoms from the trap.

Decompression

Evaporative cooling takes place in a tightly confining trap with ^{87}Rb oscillation frequencies $(\omega_x, \omega_y, \omega_z) = 2\pi \times (26, 950, 950)$ Hz. To generate the dual-species BEC images of Figs. 2 and 3, the evaporation trap was decompressed to a trap with ^{87}Rb oscillation frequencies $(\omega_x, \omega_y, \omega_z) = 2\pi \times (23, 83, 77)$ Hz through a reduction of the x-bias and y-bias fields to 20% of their evaporation value. To prepare atoms for atom interferometry, we adjust bias fields and chip currents of the evaporation trap to adiabatically displace the trap centre to the position of the Bragg beam. The confinement is also reduced, leading to Rb frequencies of $(\omega_x, \omega_y, \omega_z) = 2\pi \times (10, 25, 20)$ Hz. Before releasing the atoms, we suddenly displace the trap so as to apply a velocity kick to the atoms. Following this step, we measure the centre-of-mass velocities of the two clouds as 12.8 mm s⁻¹ for Rb and 20.7 mm s⁻¹ for K, and the cloud widths at 27 ms time of flight correspond to effective temperatures of 10 nK (Rb) and 4 nK (K).

Bragg beam

The Bragg beam is controlled by a fibre-coupled AOM, driven by the amplified output of an radiofrequency arbitrary waveform generator. This radiofrequency output drives both the AOM and the loop antenna used for radiofrequency evaporation, as selected using a switch. The arbitrary waveform generator is a National Instruments PXI-5422, capable of a monotone, dual-tone and tritone output in the range 0–80 MHz. Each atomic species requires at least two tones for two-photon Bragg diffraction: one carrier tone at the AOM resonance of 79 MHz and one offset from 79 MHz at the velocity-dependent Bragg resonance. To calibrate the Bragg interaction, we measured the Rabi rate for each Bragg transition in the dual-tone configuration. We found the $\pi/2$ pulse duration to be 0.12 ms for Rb and 0.19 ms for K. On the basis of these results, we implemented single-species Mach–Zehnder interferometers using a three-pulse $\pi/2-\pi-\pi/2$ sequence with an interrogation time (defined as the time between laser pulses) of $T = 0.5$ ms. The phase of the final pulse was scanned between 0 and 2π and the final population in the two momentum states was observed to oscillate as expected, with a visibility of approximately 0.38 for ^{87}Rb and 0.2 for ^{41}K . For simultaneous atom interferometry, the tritone provides a 79-MHz carrier with the relevant offset Bragg resonance for each species.

Imaging system

Two imaging systems are used in CAL, each supporting the collection of absorption and fluorescence images. The former are taken at the end of each experimental sequence for determining potassium and rubidium atom numbers and density profiles, whereas the latter are used to verify the proper operation of the magneto-optical trap. The circularly polarized imaging beam can be directed either along the surface of the atom chip (y axis) or through the atom-chip window (z axis). The 2D density profiles presented and analysed for this paper were collected by means of y-axis absorption imaging, with resolution at the focus measured before flight to be better than 14 μm for 780-nm light. The 8.25-mm field of view captures both the position of the atoms after decompression and the position within the centre of the Bragg beam displaced by 2 mm along the y axis. However, the relatively small depth of focus of our y-axis imaging system (calculated to be about 0.13 mm for 780-nm light) and the inability to refocus the cameras in flight resulted in moderate defocusing of the imaged atoms for both trap positions.

The imaging sequence for each atomic species constitutes two 100- μs -wide pulses that are separated by 106.3 ms. Absorption imaging of rubidium and potassium in the same experimental run interleaves these pulse sequences such that the imaging pulse for potassium is taken with 767-nm light first and the imaging pulse for rubidium is taken with 780-nm light 2.1 ms later. In Fig. 2a,b, absorption images of the ^{41}K and ^{87}Rb clouds are taken after 12 ms and 14.1 ms of free expansion time, respectively. ^{39}K is imaged in Fig. 2c after 3 ms of free expansion

time. The optical column densities and their projections along the x and z axes are also depicted and the atom numbers and cloud widths are extracted from the best 2D Gaussian fit parameters. To increase the contrast between atom clouds and background images and account for stationary interference fringes, a reference region is selected with the cloud being left outside the field of view, to scale the background images. For the fits of Fig. 3, the image quality was enhanced by principal component analysis⁶², which identifies and enhances the most substantial structures.

Dual-species interferometry analysis

The dual-species interferometer and the preparatory detuning and Rabi scans were analysed by modelling the effect of the Bragg beams^{63,64} on the momentum distribution of the atom clouds and subsequently calculating the populations in the relevant exit ports as an integral over all momenta. For the model, we have assumed initial Thomas–Fermi distributions in momentum space for both species and considered transitions only between the two resonantly coupled momentum states. The Bragg pulses are approximated as square pulses. The momentum widths $\Delta p_z = 0.142 \pm 0.008 \hbar k$ for ^{41}K and $\Delta p_z = 0.264 \pm 0.008 \hbar k$ for ^{87}Rb as well as the Rabi frequencies $\Omega = 2\pi \cdot (786 \pm 29) \text{ Hz}$ for ^{41}K and $\Omega = 2\pi \cdot (758 \pm 15) \text{ Hz}$ for ^{87}Rb were determined by fitting the model to the Rabi scan (see Extended Data Fig. 1), whereas the central momenta of the wavefunctions $p_0 = 1.779 \pm 0.004 \hbar k$ for ^{41}K and $p_0 = 2.230 \pm 0.026 \hbar k$ for ^{87}Rb were obtained through fits to the detuning scan (see Extended Data Fig. 2). Here $k = 2\pi/\lambda$ is the wavevector of the Bragg beam with wavelength $\lambda = 785 \text{ nm}$.

On the basis of these results, the expected minimum and maximum populations of the dual-species interferometer were calculated by considering the superposition of all four wavefunctions in each exit port and varying the phase of the final beam splitter between 0 and π . An extra phase of $\exp(-ip(\pm\Delta z/\hbar))$ was applied to the momentum distributions of the spurious paths of the interferometer to account for their displacement $\Delta z = 2\hbar kT/m$ in position with respect to the central paths of the interferometer. Here $T = 0.5 \text{ ms}$ is the time between the interferometer pulses and m is the mass of the atoms. The resulting bounds for the populations of the interferometer are given by $P_{\min,K} = 0.222^{+0.008}_{-0.006}$ and $P_{\max,K} = 0.493^{+0.031}_{-0.032}$ for ^{41}K and $P_{\min,Rb} = 0.230^{+0.004}_{-0.009}$ and $P_{\max,Rb} = 0.527^{+0.015}_{-0.031}$ for ^{87}Rb and are shown in Fig. 4. The values of the errors are based on the fit uncertainties of the Rabi frequency, central momentum and momentum width.

The differential phase value of $0.4^{+0.5}_{-1.2}$ was directly obtained through fitting an ellipse with five free parameters to the correlation data shown on the right-hand side of Fig. 4. The values of the errors represent the phase uncertainty of the fit and are asymmetric because of the inability to differentiate between positive and negative differential phase values.

Data availability

All NASA CAL data are on a schedule for public availability through the NASA Physical Sciences Informatics (PSI) website (<https://psi.ndc.nasa.gov/app/record/206098>) at the time of publication.

58. Ferrari, G. et al. Collisional properties of ultracold K-Rb mixtures. *Phys. Rev. Lett.* **89**, 053202 (2002).
59. Dieckmann, K. *Bose-Einstein Condensation with High Atom Number in a Deep Magnetic Trap*. PhD thesis, Universiteit van Amsterdam (2001).

60. Myatt, C. J. *Bose-Einstein Condensation Experiments in a Dilute Vapor of Rubidium*. PhD thesis, Univ. Colorado (1997).
61. Garrido Alzar, C. L., Perrin, H., Garraway, B. M. & Lorent, V. Evaporative cooling in a radio-frequency trap. *Phys. Rev. A* **74**, 053413 (2006).
62. Segal, S. R., Diot, Q., Cornell, E. A., Zozulya, A. A. & Anderson, D. Z. Revealing buried information: Statistical processing techniques for ultracold-gas image analysis. *Phys. Rev. A* **81**, 053601 (2010).
63. Siemß, J.-N. et al. Analytic theory for Bragg atom interferometry based on the adiabatic theorem. *Phys. Rev. A* **102**, 033709 (2020).
64. Jenewein, J., Hartmann, S., Roura, A. & Giese, E. Bragg-diffraction-induced imperfections of the signal in retroreflective atom interferometers. *Phys. Rev. A* **105**, 063316 (2022).

Acknowledgements We gratefully acknowledge the contributions of current and former members of CAL's operations and technical teams and those of the team at ColdQuanta. We also recognize the continuing support of JPL's Astronomy, Physics, and Space Technology Directorate, of the JPL Communications, Tracking, and Radar Division, the JPL Mission Assurance Office, the Payload Operations Integration Center (POIC) cadre at NASA's Marshall Space Flight Center, the International Space Station Program Office (ISSPO) at NASA's Johnson Space Center in Houston and ISS crew members. We are thankful for the dedicated support from the Biological and Physical Sciences Division (BPS) of NASA's Science Mission Directorate at the agency's headquarters in Washington, D.C. Finally, we appreciate the scientific guidance and discussions with CAL Principal Investigator E. Cornell, ISS Chief Scientist K. Costello, BPS Fundamental Physics Program Scientist M. Robinson and JPL Chief Scientist for Astronomy and Physics C. Lawrence. CAL was designed, managed and operated by the Jet Propulsion Laboratory, California Institute of Technology, under contract with the National Aeronautics and Space Administration (Task Order 80NM0018F0581). CAL and the Principal Investigator-led science teams, including E.R.E., D.C.A., N.P.B., S.B., J.P.D., P.E., J.R.K., J.M.K., N.E.L., N.L., M.E.M., H.M., K.O., L.E.P., C.A.S., M.S., R.J.T., and J.R.W. are sponsored by BPS of NASA's Science Mission Directorate at the agency's headquarters in Washington, D.C. and by ISSPO at NASA's Johnson Space Center in Houston. N.G., E.M.R., W.P.S., P.B., G.M. and A.P. acknowledge support by the DLR Space Administration with funds provided by the Federal Ministry for Economic Affairs and Climate Action (BMWK) under grant numbers DLR 50WM2245-A/B (CAL-II) and 50WM2253A (AI-quadrat). N.G. acknowledges support from the Deutsche Forschungsgemeinschaft (German Research Foundation) under Germany's Excellence Strategy (EXC-2123 QuantumFrontiers Grants No. 390837967) and through CRC 1227 (DQ-mat) within Project No. A05. A.P., T.E. and E.C. acknowledge support by the "ADI 2019/2022" project funded by the IDEX Paris-Saclay, ANR-11-IDEX-0003-02. HPC resources from the "Mésocentre" computing center of CentraleSupélec, École Normale Supérieure Paris-Saclay and Université Paris-Saclay was supported by CNRS and Région Île-de-France. Any opinions, findings and conclusions or recommendations expressed in this article are those of the authors and do not necessarily reflect the views of the National Aeronautics and Space Administration.

Author contributions E.R.E. conducted the experiments, analysed the data and prepared the manuscript. D.C.A. led the development, integration and testing of the upgraded science module. J.M.K. supported development of the atom-interferometry platform and led the characterization of instrument telemetry. J.R.K. led development of ISS hardware installation procedures and operations. L.E.P., M.S. and S.B. supported atom-interferometry data analysis and manuscript preparation. P.B., E.C., T.E., N.G., G.M., M.M. and A.P. modelled the mixture interactions and dual-species interferometers and supported data analysis. P.E. is a Co-Principal Investigator, E.R.E., D.C.A., J.P.D., M.E.M., H.M., E.M.R. and W.P.S. are Co-Investigators and N.P.B., N.L., C.A.S. and J.R.W. are Principal Investigators of the CAL project. The atom interferometer was proposed as a CAL add-on by the CUAS consortium including N.G., M.M., H.M., E.M.R. and W.P.S. under N.P.B. as the Principal Investigator. The inclusion of ^{39}K for studies of few-body physics in space was proposed by Co-Investigator M.E.M. and Co-Principal Investigator P.E., in collaboration with J.P.D., under Principal Investigator E. Cornell. K.O. (CAL Project Manager) and N.E.L. led technical planning across several subsystems during hardware development and science operations. R.J.T. proposed the instrument and gave scientific guidance as CAL Project Scientist from 2018 to 2020 and Cold Atom Program Scientist since 2021. J.R.W. gave scientific guidance and coordinated with Principal Investigators as CAL Project Scientist since 2021 and led the development of the atom-interferometry system. All authors read, edited and approved the final manuscript.

Competing interests The authors declare no competing interests.

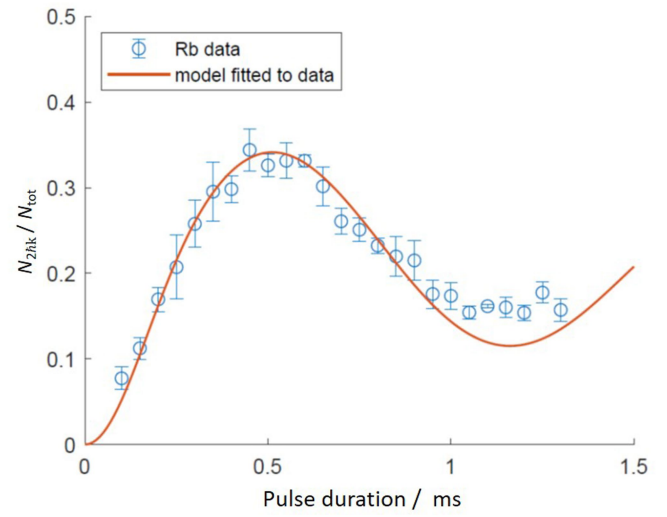
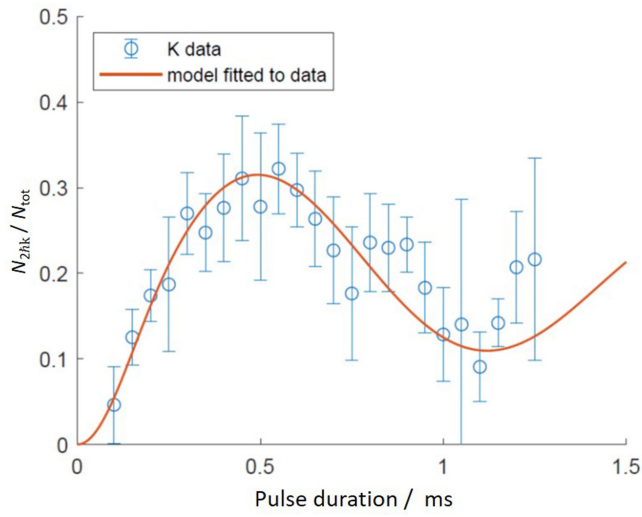
Additional information

Supplementary information The online version contains supplementary material available at <https://doi.org/10.1038/s41586-023-06645-w>.

Correspondence and requests for materials should be addressed to Ethan R. Elliott or Jason R. Williams.

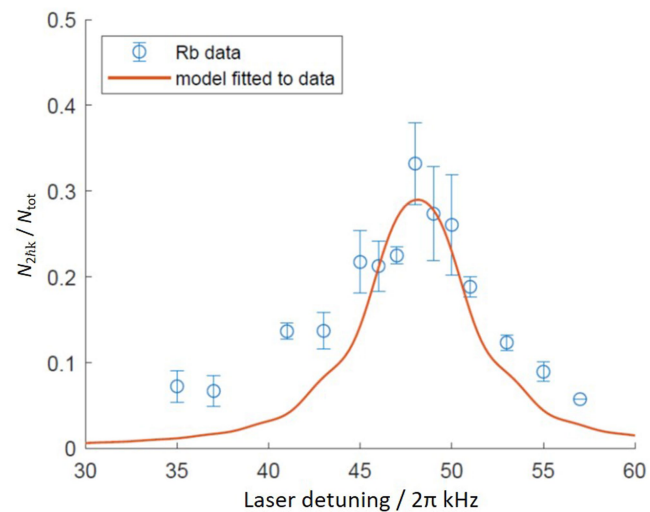
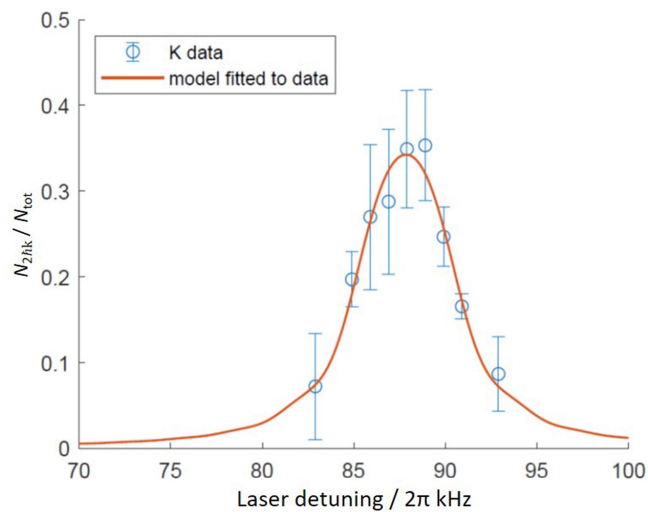
Peer review information Nature thanks Michael Holynski, Lisa Wörner and the other, anonymous, reviewer(s) for their contribution to the peer review of this work. Peer reviewer reports are available.

Reprints and permissions information is available at <http://www.nature.com/reprints>.



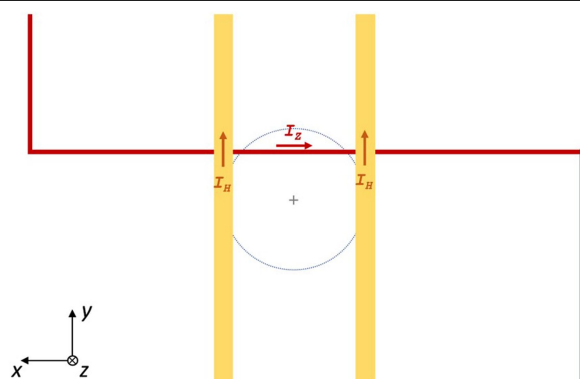
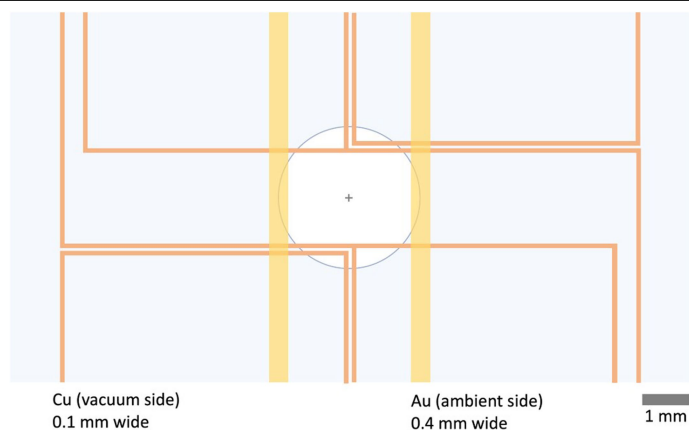
Extended Data Fig. 1 | Rabi scan. Relative population of the excited momentum state $2hk$ of a cloud of ^{41}K (left) and ^{87}Rb (right) atoms as a function of the pulse duration of a single Bragg pulse. Each data point and error bar represent the average and standard deviation, respectively, of three independent

experimental runs for a chosen pulse duration. The sequence uses the tritone configuration that was also applied in the full interferometer shown in Fig. 4. By fitting a theory model to the dataset, the Rabi frequency and the momentum width of the atom cloud was determined (see Methods).



Extended Data Fig. 2 | Detuning scan. Relative population of the excited momentum state $2\hbar k$ of a cloud of ^{41}K (left) and ^{87}Rb (right) atoms as a function of the laser detuning of a single Bragg pulse. Each data point and error bar represent the average and standard deviation, respectively, of 3–6 independent experimental runs for a chosen frequency. The sequence uses a two-tone configuration that delivers more laser power compared with the full

interferometer shown in Fig. 4, but can only address a single atomic species in each run. By fitting a theory model to the dataset, the central detuning of the atom cloud and an adjusted Rabi frequency was determined, as explained in Methods. Owing to the difference in laser power, the Rabi frequency obtained from this measurement was not used to model the full interferometer.



Extended Data Fig. 3 | Atom-chip layout of science module SM3. Left, layout of the atom chip in the upgraded science module, designated SM3. The chip surface is a silicon wafer that is anodically bonded to the glass walls of the vacuum chamber to form the top wall. Current-carrying traces on the vacuum side of the chip are made of copper (orange), whereas traces on the ambient side are made of gold (yellow). A 3-mm-diameter antireflection-coated glass window in the centre allows for beam propagation through the chip surface, for both imaging and Bragg interferometry. Right, the traces used in this work.

During evaporation, I_z and I_H carry 2.4 A and 2.3 A, respectively, in the directions indicated, which combine with bias fields in the x , y and z directions of -9.3 , 35.2 and -1.7 G to form a magnetic trap with ^{87}Rb oscillation frequencies of $(\omega_x, \omega_y, \omega_z)/2\pi = (26, 950, 950)$ Hz. To displace the atom-trap centre to the centre of the window and overlap with the Bragg beam, chip currents are adiabatically ramped to I_z and I_H values of 2.1 A and 0.7 A, whereas the bias fields ramp to 0, 1.88 and -2.05 G to give a trap with Rb frequencies of $2\pi \times (10, 25, 20)$ Hz.